

Full length article



Free Vibration analysis of C/SiC blisk based on modified global mode method

Qian Xu ^a, Lei Hou ^{a,*}, Lixian Hou ^b, Zhonggang Li ^a, Shuangxing Ren ^a, Mohamed K. Aboudaif ^e,
Emad Mahrous Awwad ^f, Nasser A. Saeed ^{a,c,d,g}

^a School of Astronautics, Harbin Institute of Technology, Harbin, 150001, PR China

^b Shanghai Space Propulsion Technology Research Institute, Shanghai, 201109, PR China

^c Department of Physics and Engineering Mathematics, Faculty of Electronic Engineering, Menoufia University, Menoufia, 32952, Egypt

^d Mathematics Department, Faculty of Science, Galala University, Galala City, 43511, Egypt

^e Raytheon Chair for Systems Engineering (RCSE), Advanced Manufacturing Institute, King Saud University, Riyadh, 11421, Saudi Arabia

^f Department of Electrical Engineering, College of Engineering, King Saud University, P.O. Box 800, Riyadh, 11421, Saudi Arabia

^g Jadara University Research Center, Jadara University, P.O.Box:733, Irbid, 21110, Jordan

ARTICLE INFO

Keywords:

Blisk
Modified global mode method
Semi-analytical method
2D C/SiC materials
Free Vibration

ABSTRACT

The bladed disk is the core component which is under load in aero-engine, rocket engine and gas turbine. In recent years, the bladed disk has developed towards the direction of integrated bladed disk (blisk) and being applied with ceramic matrix composites. However, there is no accurate semi-analytical dynamic model to describe the dynamic characteristic of ceramic matrix composite blisk. In this paper, a new semi-analytical method, modified global mode method (MGMM) is proposed to model the 2D C/SiC laminated blisk. In proposed method, Chebyshev polynomials series are used to expand the displacements of the blades and disk, constraints between blades and disk is strictly satisfied by multi-modal transformation and integrated into governing equation, and high-order shear deformation theory is combined to establish the dynamic model of the blisk of 2D C/SiC laminated composite material. The proposed method avoids the matrix singular problem appearing in traditional global mode method when modeling of combined structure and makes the system perform dynamic analysis and mode prediction without mode extraction and reconstruction. Then, amplitude frequency response and modal experiment are carried out to verify the correctness and convergence of the proposed method. Finally, under the framework of proposed method, the effects of material parameters and geometric parameters on the modal characteristics of the blisk are analyzed. The results show that compared with the geometric parameters, the material parameters have less influence on the modal characteristics of blisk, additionally, a series of modal steering is observed. The work in this paper can provide theoretical guidance for the dynamic design of composite blisk.

1. Introduction

As the core component of aero-engine and rocket engine, the bladed disk bears a variety of extreme loads during the operation of the engine, and plays an important role in the safe operation of the aircraft [1–3]. Therefore, the dynamic characteristics of the bladed disk is a factor that must be considered in the design of modern engines. Especially in recent years, the bladed disk structure has gradually developed towards the direction of integrated forming of the bladed disk structure (blisk) [4,5] and being applied with advanced ceramic matrix composites [6], resulting that the lightweight, low damping and more severe vibration. Therefore, it has important guiding significance to investigate the vibration characteristics of the ceramic matrix composite blisk.

In the current studies of the dynamic characteristics of the bladed disk, three methods are generally used for the dynamic modeling of the bladed disk, namely lumped parameter method [7–10], finite element method (FEM) [11] and semi-analytical method based on Rayleigh Ritz method [12]. The precision of the lumped-parameter method is low and the error is large, the finite element method has the advantages of high analysis accuracy but also has excessive degrees of freedom and excessive analysis cost [13], especially for the bladed disk structure. The semi-analytical method has the characteristics of clear mechanical mechanism, low computational cost and high reliability so it is reasonable to use the semi-analytical method to study the blisk.

For combined structures like blisk, introducing artificial springs between each sub-structure to realize the connection of the structures is the most common semi-analytical modeling method [14–16].

* Corresponding author.

E-mail address: [houlei@hit.edu.cn](mailto:houlel@hit.edu.cn) (L. Hou).

URL: <http://homepage.hit.edu.cn/houlel> (L. Hou).

<https://doi.org/10.1016/j.tws.2024.112285>

Received 30 May 2024; Received in revised form 30 June 2024; Accepted 29 July 2024

Available online 31 July 2024

0263-8231/© 2024 Elsevier Ltd. All rights are reserved, including those for text and data mining, AI training, and similar technologies.

Tomioka [17] introduced two artificial springs of displacement and rotation angle at the root of the blade to complete the modeling of bladed disk, and then Gao et al. [12,18] and Chen et al. [19] used this method to investigate the modal, damping characteristics and forced vibration of blisk with blade coating. The advantage of this method is that, it is easy to implement and the resulting error is within an acceptable range, however it is not suitable for the blisk structure because it cannot strictly satisfy the continuity of the deformation of the blades and disk.

Another widely used semi-analytical method for bladed disk in recent years employs the coordinate transformation between sub-structures to complete the modeling, and each sub-structure can be regarded as a simple support case (such as fixed support) in its own coordinate system [20]. Wu et al. [21] adopted this method when studying the influence of blade cracks on the modal characteristics of the bladed disk with elastic support, both the disk and blades can be regarded as fixed support in their own coordinate system, additionally, Wu et al. also used this method to study the modal characteristics of the flexible dual-rotor system with blade cracks [22]. Based on this method, Chiu et al. [23] studied the vibration of the coupled rotor with multiple blades, Chun et al. [24] studied the coupled vibration of the shaft, disk and blades, and She et al. [25] analyze the frequency steering and merging of the bladed disk system. Zhao et al. [26,27] investigated the free coupling vibration of composite bladed disk, and Zhou et al. [28] studied the vibration characteristics of a flexible blade-disk-rotor system with lines by combining the assumed mode method and the finite element method. This method can automatically and strictly satisfy the deformation continuity of blade and disk. However, none of research objects of these literature narrated in this paragraph are integrated blisk models, and even because the transformation matrix between the coordinate systems is a function of generalized variables, the energy of the system is not a standard quadratic form when using Rayleigh-Ritz method, thus necessary Taylor expansion and linearization are needed.

In order to solve the common dynamic modeling problem of combined structure in engineering, the global mode method(GMM) based on principle of minimum potential energy comes into being. In this method, each sub-structure is modeled separately from the global perspective, the Lagrange multipliers are introduced to meet the constraints, and the dynamic modeling of combined structure is finally completed. Liu et al. [29] studied the generalized analytical modes of spacecraft with three-axis stability, Wei et al. [30] studied the dynamic modeling problem of flexible manipulator with concentrated mass, and for the dynamic problem of solar panel of satellite, Cao, Wei et al. and He et al. [31–34] studied a series of related vibration problems of solar panel based on GMM with Rayleigh Ritz method, such as the modeling of multi-plate solar sail with flexible hinges, dynamic response and vibration control problem, Tian et al. [35] also used GMM with Rayleigh Ritz method to investigate the aeroelasticity problem of folding wing with multi-plate structure. The GMM based on Rayleigh-Ritz is very suitable for the dynamic modeling of the integrated combined structure, but it needs a mode extraction and reconstruction to calculate the dynamic response after modeling, because the characteristic equation of the system becomes singular after introducing the Lagrange multiplier.

With high specific modulus, low density and excellent high temperature performance, ceramic matrix composites(CMCs) are more and more used in high temperature components in the aeronautics and astronautics [36–41], including turbine rotors of aero-engine and rocket engine. In recent years, there have been a considerable number of literature reports on the application of ceramic matrix composites on blades and blade disks. Min et al. [42] studied the problem of damping characterization of C/SiC materials applied to turbine blade disks, Kumar et al. [43] studied the problem of damage and destruction of CMCs blades and disk, Langenbrunner et al. [44] studied the dy-

amic response of turbine blades under controlled rub conditions. As a typical braided ceramic matrix composite, 2D C/SiC is used in many components of the engine [45–47]. However, there is no literature on dynamic modeling and dynamic characteristic analysis of 2D C/SiC blisk.

From the above mentioned literatures, it can be seen that the existing two mainstream semi-analytical modeling methods are not fully applicable to composite blisk, and it is necessary to develop a reasonable and highly reliable modeling method for blisk, obviously the global mode method is the best choice, but the singularity problem of the global mode method also needs to be solved. In addition, CMCs are increasingly used in high temperature parts of engines, and there are few literature on CMCs blisk.

The motivation of this paper is to improve the modeling method which is suitable for composite blisk, overcome the shortcoming of singularity of the dynamic equation based on traditional GMM, and detect the effect of parameters of 2D C/SiC blisk on modal characteristic. A modified global mode method is proposed in this paper, where the connection of blades and disk based on displacement continuity is given in the form of constraint equations and is integrated into the final coupled dynamic equation by multi-modal transformation. The elastic constants of single-layer 2D C/SiC composites are obtained using the stiffness averaging method. Combining high-order shear deformation theory and Chebyshev polynomials, the displacement of 2D C/SiC blisk is constructed. The final dynamic equation of composite blisk is given based on the Hamilton principle. Then, the finite element simulation and experiments are performed to verify the correctness of the proposed method in this paper. Further parametric analysis is carried out to investigate the effect of geometric parameters and materials parameters of 2D C/SiC composite on modal characteristic. Moreover, the results of this paper can provide theoretical guidance for the dynamic design and vibration control of C/SiC composite blisk.

2. Mechanical model of blisk based on modified global mode method

In this section, the global modal method is improved and modified(named Modified Global Mode Method, MGMM), and used to establish the dynamic model of the blisk system. The blisk system is illustrated in Fig. 1, the disk is simplified as the annular plate, whose the inner edge is clamped while the outer edge is free and connected with the blades. The geometry information of the disk is shown in Fig. 1a with thickness h^d , inner radius R^{in} , outer radius R^{out} . The blades are simplified as 3D beams which are connected with the outer edge of the disk, its geometry information, blade span l^b , blade chord b^b , thickness h^b and pre-setting angle β are shown in Fig. 1b and c, as well as the transformation relationship between the Cartesian coordinate $o_i \xi_i v_i \eta_i$ of No. i blade and cylindrical coordinate $Or\theta z$ of the disk.

Both the blade and the disk are consist with a number of layers of 2D braided C/SiC materials, which is shown in Fig. 2. Single layer is 2D braided composite with C fiber and SiC matrix. In this paper, it is defined that the material of the blade disk of the blade is exactly the same, that is, the number of layers and the laying angles are exactly the same.

2.1. 2D C/SiC laminated model

It can be seen from Fig. 2c that, the micro-structure of 2D C/SiC is periodic spatially, so the macroscopic elastic constant of the whole materials can be replaced and characterized by the elastic constant of the representative volume Element(RVE), which is the smallest repeating unit in space.

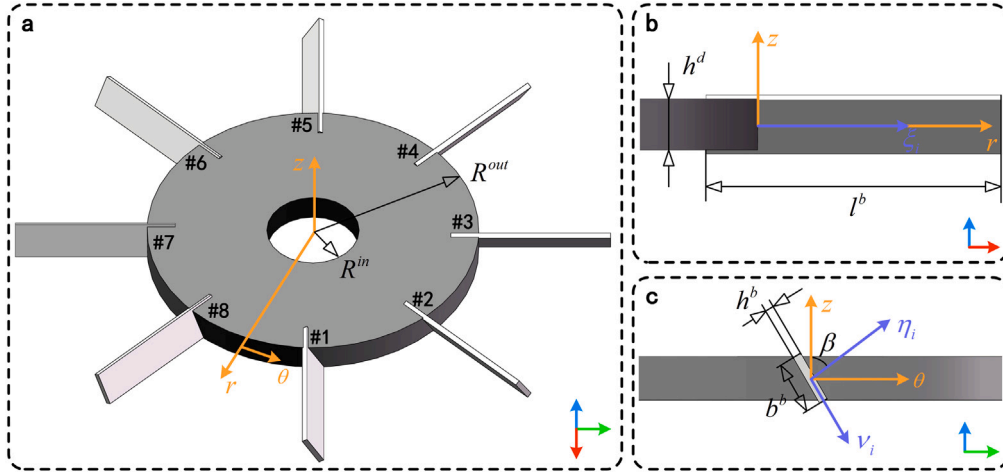


Fig. 1. Schematic diagram of the disk with 8 blades. a: cylindrical coordinate of the disk and its geometry information b and c: Cartesian coordinate of the No. i blade and its geometry information.

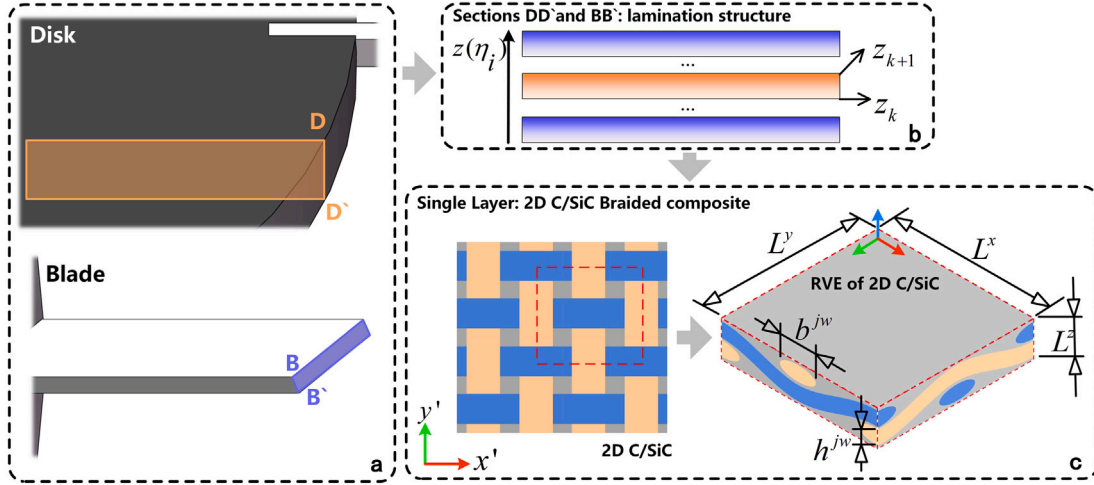


Fig. 2. Schematic diagram of the disk with 8 blades. a and b: laminated structure sections of disk and blade c: 2D C/SiC in single layer.

2.1.1. Micro-mechanical model of C/SiC composite of disk and blades

The RVE of single-layer 2D C/SiC composite is shown in Fig. 2c, which shows the geometry information of warp, weft and RVE. The sections of the warp and weft are assumed to be elliptical, and the lengths of the major and minor axes are respectively b^{jw} , h^{jw} . The dimensions of RVE in the three dimensions are L^x , L^y , L^z , obviously $L^x = L^y$. It should be pointed out that L^x and L^y of RVE are related to the yarn arrangement density of warp and weft [48], i.e.

$$L^x = L^y = \frac{2}{M^{jw}} \quad (1)$$

where M^{jw} is the warp and weft arrangement density (tows/mm) which determines the distance between adjacent two yarns.

It can be seen from Fig. 2 that, the laying curve of the warp and weft in RVE is assumed to be a sine function, i.e.

$$z' = d^{jw} \sin\left(\frac{2\pi}{L^x} x' - \frac{\pi}{2}\right) \quad (2)$$

where d^{jw} determines the amplitude of the yarn motion. thus the length of single yarn (warp and weft) is

$$l^{jw} = \int_0^{L^x} \sqrt{1 + \left(\frac{dz'}{dx'}\right)^2} dx' \quad (3)$$

the volume fractions of warp, weft and matrix are

$$\begin{cases} v^j = \frac{\pi b^{jw} h^{jw} l^{jw}}{2L^x L^y L^z} \\ v^w = v^j \\ v^m = 1 - v^j - v^m \end{cases} \quad (4)$$

2.1.2. Volume average

The volume averaging method is used to obtain the macroscopic elastic constants of single-layer 2D C/SiC composites, i.e.

$$[C^{RVE}] = v^j [C^j] + v^w [C^w] + v^m [C^m] \quad (5)$$

where the $[C^{RVE}]$ is the stiffness matrix of RVE in $o'x'y'z'$; the $[C^j]$, $[C^w]$, $[C^m]$ are the stiffness matrix of warp, weft, matrix in $o'x'y'z'$; v^j , v^w , v^m are the volume fraction of warp, weft, matrix.

Warp and weft are laid in the RVE in the form of a sine curve, so their stiffness in $o'x'y'z'$ can be obtained by (the only difference between warp and weft is the laying direction, so taking the warp for example)

$$[C^j] = \left[\frac{1}{l^{jw}} \int_0^{l^{jw}} [T^j(s)]^T [S^{j*}] [T^j(s)] ds \right]^{-1} \quad (6)$$

where the l^{jw} is the length of the single warp in RVE, $[T^j(s)]$ is the transformation matrix between the warps body coordinate system and $o'x'y'z'$, which is obviously a function by arc coordinates s , and $[S^{j*}]$ is the flexibility Matrix in the fiber body coordinate system.

$[C^m]$ is easily obtained by inverting its flexibility matrix, i.e. $[C^m] = [S^m]^{-1}$. After the stiffness matrix of RVE is obtained by Eq. (5), its flexibility matrix can be obtained by inverting, $[S^{RVE}] = [C^{RVE}]^{-1}$, thus, the Elastic Constants can be obtained by

$$\begin{cases} E_{11} = \frac{1}{S_{11}} \\ E_{22} = \frac{1}{S_{22}} \\ \nu_{12} = -\frac{S_{12}}{S_{11}} \\ G_{12} = \frac{1}{S_{66}} \\ G_{23} = \frac{1}{S_{44}} \\ G_{13} = \frac{1}{S_{55}} \end{cases} \quad (7)$$

where, E_{11} and E_{22} are the equivalent stretch modulus along the x' and y' directions, respectively, ν_{12} is the Poisson's ratio in the $x'y'$ plane, and G_{12} , G_{23} and G_{13} is the shear modulus of $x'y'$, $y'z'$ and $x'z'$.

Only the above elastic parameters are needed in this analysis, so elastic constants other than these are not listed. From the modeling of the micro-structure of 2D C/SiC in this subsection, it can be seen that the elastic constants of the material along the x' and y' directions are consistent in the $o'x'y'z'$ coordinate.

Density of disk and blade is also averaged by volume, i.e.

$$\rho^d = \rho^b = (\nu^j + \nu^w) \rho^f + \nu^m \rho^m \quad (8)$$

where the ρ^f is the density of warp and weft, and ρ^m is the density of SiC matrix and them are listed in Appendix.

2.2. Dynamic model of the disk

The displacement of the disk in its cylindrical coordinate system $Or\theta z$ is described by the high order shear deformation theory (HSDT) in order to more accurately describe the shear deformation of composite disk and its larger thickness, which is written in matrix form as follow.

$$\{U\} = \begin{Bmatrix} U^1 \\ U^2 \\ U^3 \end{Bmatrix} = \begin{bmatrix} -c^d z^3 \partial_r & z - c^d z^3 \\ -z \frac{1}{r} \partial_\theta & 0 \\ r & 0 \end{bmatrix} \begin{Bmatrix} U^z \\ U^\phi \end{Bmatrix} \quad (9)$$

where $U^i, i = 1, 2, 3$ are the displacement of an arbitrary point (r, θ, z) in the annular plate along the direction r, θ and z , respectively; U^z is the displacement of an arbitrary point (r, θ) of neutral plane of plate along the direction z ; U^ϕ is the rotational angle of neutral surface in the annular plate around the axis θ ; $\partial_i, i = r, \theta$ is the partial differential operator, and constant $c^d = \frac{4}{3(h^d)^2}$.

The relationship between displacement and strain is

$$\{\epsilon^U\} = \begin{Bmatrix} \epsilon_{rr}^U \\ \epsilon_{\theta\theta}^U \\ \epsilon_{\theta z}^U \\ \epsilon_{rz}^U \\ \epsilon_{r\theta}^U \end{Bmatrix} = \begin{Bmatrix} \frac{\partial U^1}{\partial r} \\ \frac{1}{r} U^1 + \frac{1}{r} \frac{\partial U^2}{\partial \theta} \\ \frac{1}{r} \frac{\partial U^3}{\partial \theta} + \frac{\partial U^2}{\partial z} \\ \frac{\partial U^1}{\partial z} + \frac{\partial U^3}{\partial r} \\ \frac{1}{r} \frac{\partial U^1}{\partial \theta} + \frac{\partial U^2}{\partial r} - \frac{1}{r} U^2 \end{Bmatrix} \quad (10)$$

The elastic equation of the disk of k th can be written as

$$\{\sigma_k^U\} = [Q_k^U(\alpha_k^d)] \{\epsilon^U\} \quad (11)$$

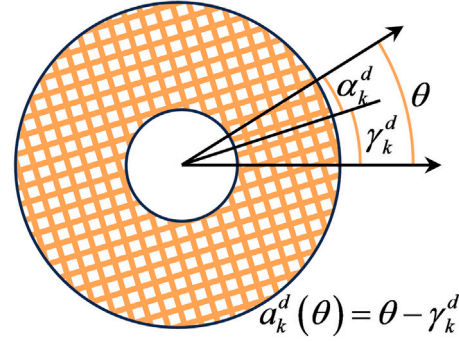


Fig. 3. Schematic diagram of laying angle of yarns in disk.

where the $[Q_k^U]$ is the elastic stiffness matrix of k th Layer, which is obtained by transformation of Eq. (7). It is worth being noted that, laying angle of k th referring to the radial axis is a function of θ , i.e. $\alpha_k^d = \theta - \gamma_k^d$ (shown in Fig. 3), due to the rotation angle between the polar diameter and the principal direction of the material. Details in Calculation of $Q_k^U(\alpha_k)$ refs to [49].

Considering all layers share the same density, the Kinetic Energy of the rotating disk is

$$T^U = \frac{1}{2} \rho^d \int_{-h^d/2}^{h^d/2} \int_0^{2\pi} \int_{R^{in}}^{R^{out}} \left[(U^1 - \omega U^2)^2 + (U^2 + \omega(U^1 + r))^2 + (U^3)^2 \right] r dr d\theta dz \quad (12)$$

where ω is the rotational speed. The potential Energy of the disk is

$$V^U = \frac{1}{2} \sum_{k=1}^K \int_{z_{k-1}}^{z_k} \int_0^{2\pi} \int_{R^{in}}^{R^{out}} \{\sigma_k^U\}^T \{\epsilon^U\} r dz d\theta dr + \int_{-h^d/2}^{h^d/2} \int_0^{2\pi} \int_{R^{in}}^{R^{out}} \left[f^{rc} \left(\frac{\partial U^z}{\partial r} \right)^2 + f^{\theta c} \left(\frac{1}{r} \frac{\partial U^z}{\partial \theta} \right)^2 \right] r d\theta dr dz \quad (13)$$

where f^{rc} and $f^{\theta c}$ is the centrifugal force [22]. The first term in the Eq. (13) is strain potential energy and the second term is the centrifugal potential energy due to the rotation.

2.3. Dynamic model of the blades

The displacement of the i th blade in its Cartesian coordinate $o_i \xi_i \nu_i \eta_i$ is also described by the HSDT, which is written in matrix form as follow.

$$\{u_i\} = \begin{Bmatrix} u_i^1 \\ u_i^2 \\ u_i^3 \end{Bmatrix} = \begin{bmatrix} 0 & -c^b \eta_i^3 \partial_{\xi_i} & \eta_i - c^b \eta_i^3 \\ 1 & 0 & 0 \\ 0 & 1 & 0 \end{bmatrix} \begin{Bmatrix} u_i^\nu \\ u_i^\eta \\ u_i^\phi \end{Bmatrix} \quad (14)$$

where u_i^1, u_i^2, u_i^3 is the displacement of the blade along the direction ξ_i, ν_i and η_i , respectively, u_i^ν and u_i^η is the displacement of neutral line in the blade along the direction ν_i and η_i ; u_i^ϕ is the rotational angle of neutral line around the axis ξ_i , and $c^b = \frac{4}{3h^b^2}$. Noting that the displacement

along the chord direction u_i^ν is rigid body displacement because the chord bending stiffness of a blade is much higher than its transverse bending stiffness, and u_i^ν is introduced only to match the displacement between the blade and disk, its contribution to blade potential energy should be ignored.

The strain of the blade is

$$\{\epsilon_i^u\} = \begin{Bmatrix} \epsilon_{i,\xi\xi}^u \\ \epsilon_{i,\nu\xi}^u \end{Bmatrix} = \begin{Bmatrix} \frac{\partial u_i^1}{\partial \xi_i} \\ \frac{\partial u_i^1}{\partial \eta_i} + \frac{\partial u_i^3}{\partial \xi_i} \end{Bmatrix} \quad (15)$$

The stress of the blade is

$$\{\sigma_{ik}^u\} = \begin{bmatrix} E_k^b(\gamma_k^b) & 0 \\ 0 & G_k^b(\gamma_k^b) \end{bmatrix} \{\varepsilon_i^u\} \quad (16)$$

where the E_k^b, G_k^b are elastic constants of the blade, γ_k^b is the laying angle of k th layer referring to axis ξ_i , see [50] for the method of calculating the elastic constants E_k^b and G_k^b .

The position vector of arbitrary point of i th blade in global view is

$$\{P_i^b\} = \begin{bmatrix} \cos \omega t & -\sin \omega t & 0 \\ \sin \omega t & \cos \omega t & 0 \\ 0 & 0 & 1 \end{bmatrix} \begin{bmatrix} 1 & 0 & 0 \\ 0 & \cos \beta & -\sin \beta \\ 0 & \sin \beta & \cos \beta \end{bmatrix} \begin{Bmatrix} R^b + \xi_i + u_i^1 \\ u_i^2 \\ \eta_i + u_i^3 \end{Bmatrix} \quad (17)$$

thus, the Kinetic Energy of the rotating i th blade is

$$T_i^u = \frac{1}{2} \rho^b \int_{-h^b/2}^{h^b/2} \int_0^{l^b} \{\dot{P}_i^b\}^T \{\dot{P}_i^b\} b^b d\eta_i d\xi_i \quad (18)$$

The potential Energy of the blade is

$$V_i^u = \frac{1}{2} \sum_{k=1}^K \int_{\eta_i(k-1)}^{\eta_{ik}} \int_0^{l^b} \{\varepsilon_i^u\}^T \{\sigma_{ik}^u\} b^b d\eta_i d\xi_i + \frac{1}{2} \int_{-h^b/2}^{h^b/2} \int_0^{l^b} f^{\xi c}(\xi_i) \left[\left(\frac{\partial u_i^3}{\partial \xi_i} \right)^2 + \left(\frac{\partial u_i^2}{\partial \xi_i} \right)^2 \right] b^b d\eta_i d\xi_i \quad (19)$$

where $f^{\xi c}(\xi_i)$ is the centrifugal force, written as

$$f^{\xi c}(\xi_i) = \rho^b \omega^2 \left[R^{out} (l^b - \xi_i) + \frac{l^b{}^2 - \xi_i^2}{2} \right] \quad (20)$$

2.4. Final governing equation based on modified global mode method

The key of the global mode method(GMM) is to satisfy the geometric boundary conditions of each substructure in the global view. For the disk, it is clamped on inner edge and free on the outer edge. For the blade, it is both free on the top and the bottom.

The displacement of the neutral surface of the disk in Eq. (9) can be expressed in the general product form of the shape function and generalized displacement, i.e.

$$\begin{Bmatrix} U^z \\ U^\phi \end{Bmatrix} = \begin{bmatrix} \{N^{U^z}\}^T & 0 \\ 0 & \{N^{U^\phi}\}^T \end{bmatrix} \begin{Bmatrix} \{q^{U^z}\} \\ \{q^{U^\phi}\} \end{Bmatrix} = [N^U] \{q^U\} \quad (21)$$

where the $\{N^i\}, i = U^z, U^\phi$ is the shape function vector, and $\{q^i\}, i = U^z, U^\phi$ is the generalized displacement vector. Noting that the shape function must satisfy the geometry boundary condition mentioned in the above, i.e. the displacement of the disk must be 0 at $r = R^{in}$, so the shape function could be determined as following

$$\begin{cases} \{N^{U^z}\}_{(m-1)(2J^{U^z}+1)+n} = h^d P_m^*(r) T_n(\theta), m = 1, 2 \dots I^{U^z}, n = 1, 2 \dots 2J^{U^z} + 1 \\ \{N^{U^\phi}\}_{(m-1)(2J^{U^\phi}+1)+n} = P_m^*(r) T_n(\theta), m = 1, 2 \dots I^{U^\phi}, n = 1, 2 \dots 2J^{U^\phi} + 1 \end{cases} \quad (22)$$

where $P_m^*(r)$ is the No. m Chebyshev polynomials of 2nd in the region $[R^{in}, R^{out}]$ which satisfy $P_m^*(R^{in}) = 0$. For the construction of the Chebyshev polynomials of 2nd for different boundary conditions, refer to [51]. $\{T(\theta)\}$ stands for the circumferential traveling wave function vector of the disk, which is written as

$$\{T\} = \{1, \cos \theta, \cos 2\theta, \dots \cos s\theta, \sin \theta, \sin 2\theta, \dots \sin s\theta\} \quad (23)$$

where s is the traveling wave number, and obviously, $s = J^{U^z}$ or J^{U^ϕ} .

In HSDT used in this paper, the rotational angle of the plate around the θ axis is independent of the lateral deflection, so not ‘‘Clamped-Free’’ but ‘‘Simply supported-Free’’ condition can be taken when deciding the radial shape function $P_m^*(r)$ in Eq. (22).

The displacement of the blade is expanded, which is the same as the previous process of expansion the displacement of the disk, i.e.

$$\begin{Bmatrix} u_i^v \\ u_i^n \\ u_i^\phi \end{Bmatrix} = \begin{bmatrix} \{N_i^{u^v}\}^T & 0 & 0 \\ 0 & \{N_i^{u^n}\}^T & 0 \\ 0 & 0 & \{N_i^{u^\phi}\}^T \end{bmatrix} \begin{Bmatrix} \{q_i^{u^v}\} \\ \{q_i^{u^n}\} \\ \{q_i^{u^\phi}\} \end{Bmatrix} = [N_i^u] \{q_i^u\} \quad (24)$$

where $\{N_i^{u^v}\}, \{N_i^{u^n}\}$ and $\{N_i^{u^\phi}\}$ are the shape function vectors of the blades, and they should satisfy the geometry condition as free in $\xi_i = 0$ and $\xi_i = l^b$. Thus the three shape function vectors share the same set of ‘‘Free-Free’’ orthogonal polynomial, written as

$$\begin{cases} \{N_i^{u^v}\}_m = h^b P_m(\xi_i), m = 1, 2 \\ \{N_i^{u^n}\}_m = h^b P_m(\xi_i), m = 1, 2 \dots I^{u^n} \\ \{N_i^{u^\phi}\}_m = P_m(\xi_i), m = 1, 2 \dots I^{u^\phi} \end{cases} \quad (25)$$

where $P_m(\xi_i)$ is No. m the Chebyshev polynomials of 2nd in the region $[0, l^b]$ which is both free in $\xi_i = 0$ and $\xi_i = l^b$. It should be pointed out that $\{N_i^{u^v}\}$ in Eq. (25) takes the first two orders because only the first two orders of the shape function of ‘‘Free-Free’’ are rigid body displacement, as mentioned above.

After the shape function of the disk and blade are determined, it can be seen that the blades are totally free in the global view, so it is necessary to introduce the constraint conditions between the disk and blades. It can be seen in Fig. 1 that there are N_b nodes where the N_b blades connect with disk, which can be written in coordinate $Or\theta z$ and $o_{\xi_i}^b v_i \eta_i$

$$\begin{cases} \Gamma_0 = (0, 0, 0) & \text{in } o_i \xi_i v_i \eta_i, \quad i = 1, 2 \dots N_b \\ \Gamma_i = \left(R^{out}, \frac{2\pi(i-1)}{N_b}, 0 \right) & \text{in } Or\theta z, \quad i = 1, 2 \dots N_b \end{cases} \quad (26)$$

The following 4 constraint equations are introduced to ensure that the displacement and rotational angle of the blade and disk are continuous at the connect points

$$\begin{cases} \text{Displacement continuity:} & \begin{cases} U^z|_{\Gamma_i} - \sin \beta u_i^v|_{\Gamma_0} - \cos \beta u_i^n|_{\Gamma_0} = 0 \\ -\cos \beta u_i^v|_{\Gamma_0} + \sin \beta u_i^n|_{\Gamma_0} = 0 \end{cases} \\ \text{Angle continuity:} & \begin{cases} U^\phi|_{\Gamma_i} + \sin \beta \frac{\partial u_i^v}{\partial \xi_i}|_{\Gamma_0} - \cos \beta u_i^\phi|_{\Gamma_0} = 0 \\ \cos \beta \frac{\partial u_i^v}{\partial \xi_i}|_{\Gamma_0} + \sin \beta u_i^\phi|_{\Gamma_0} = 0 \end{cases} \end{cases} \quad (27)$$

where, the first two constraints ensure that the lateral and circumferential displacement of the blade and disk are continuous, and the last two constraints ensure that the lateral and circumferential angles of the blade and disk are continuous. Noting that, rotational angle in HSDT is the opposite of the rotational angle defined in classical plate theory in terms of the first derivation of the lateral displacement.

By substituting Eqs. (21) and (24) into Eq. (28), Eq. (28) can be rewritten into matrix form, i.e.

$$\begin{cases} [C_1] \{ \{q^U\}^T, \{q_i^u\}^T \}^T = \{0\} \\ [C_2] \{ \{q^U\}^T, \{q_i^u\}^T \}^T = \{0\} \\ [C_3] \{ \{q^U\}^T, \{q_i^u\}^T \}^T = \{0\} \\ [C_4] \{ \{q^U\}^T, \{q_i^u\}^T \}^T = \{0\} \end{cases} \quad (28)$$

where $[C_j], j = 1, 2, 3, 4$ are the constraint matrices corresponding to the four constraints in Eq. (28), respectively.

The previous literature using GMM based on Rayleigh–Ritz method almost adopted the method of introducing Lagrange multipliers and extending the dimension of the original system to meet the displacement constraints in order to obtain the modal characteristics of the combined structure, which not only increases the degree of freedom of the system, but also leads to the singularity of the mass matrix. In

order to solve this problem, the global modal method is improved and modified in this paper. The original modal space is transformed into generalized modal space by orthogonal transformation, and then the constrained generalized modal freedom is eliminated in the generalized modal space due to the constraints. Eq. (28). The specific process is as follows.

When the constraints are not considered and no external excitation doing work, the Hamiltonian of the system with incomplete constraints is

$$\Pi = V^U + \sum_{i=1}^{N_b} V_i^u - T^U - \sum_{i=1}^{N_b} T_i^u \quad (29)$$

The virtual work of the system due to external load doing work is $\delta W = \delta W^U + \sum_{i=1}^{N_b} \delta W_i^u$, where

$$\begin{cases} \delta W^U = \int_{-h^d/2}^{h^d/2} \int_{R^{in}}^{R^{out}} \int_0^{2\pi} (\delta U^z F^{Uz} + \delta U^\phi F^{U\phi}) r dr d\theta dz \\ \delta W_i^u = \int_{-h^b/2}^{h^b/2} \int_0^{l^b} (\delta u_i^v F_i^{uv} + \delta u_i^\eta F_i^{u\eta} + \delta u_i^\phi F_i^{u\phi}) b^b d\xi_i d\eta_i \end{cases} \quad (30)$$

and, F^{Uz} , $F^{U\phi}$, F^{uv} , $F^{u\eta}$ and $F^{u\phi}$ is the generalized force applying in corresponding displacement.

based on Hamilton principle

$$\int_{t_0}^{t_1} \delta \Pi + \delta W dt = 0 \quad (31)$$

the governing equation of the system without constraints is

$$[M] \{\ddot{q}\} + [D] \{\dot{q}\} + [K] \{q\} = \{F\} \quad (32)$$

where $\{q\} = \left\{ \{q^U\}^T, \{q_i^u\}^T \right\}^T$, $i = 1, 2 \dots N_b$, $[M]$, $[D]$, $[K]$ is the mass, damping (gyroscopic) and stiffness matrix including structural stiffness and additional stiffness due to rotation, respectively, and $\{F\}$ is the external load in mode space. Obviously there is no coupling between disk and blades in Eq. (32). Constraints in Eq. (28) are introduced in order to transform the original system into a fully constrained system. Eq. (28) are assembled into

$$\begin{bmatrix} [C_1] \\ [C_2] \\ [C_3] \\ [C_4] \end{bmatrix} \{q\} = [C] \{q\} = \{0\} \quad (33)$$

obviously, the above constraint equation can be invertible transformed into

$$[C] [T]^T [T] \{q\} = [\bar{C}] \{\bar{q}\} = \begin{bmatrix} [\bar{C}^D] & [\bar{C}^I] \end{bmatrix} \begin{Bmatrix} \{\bar{q}^D\} \\ \{\bar{q}^I\} \end{Bmatrix} = \{0\} \quad (34)$$

where $[T]$ is orthogonal matrix, which makes the $[\bar{C}^D]$, the first sub-square matrix of $[\bar{C}]$ is full-rank, $\{\bar{q}\}$ is named as generalized modal coordinates in order to distinguish from ordinary modal coordinates $\{q\}$. Obviously, sub-vector $\{\bar{q}^D\}$ in $\{\bar{q}\}$ is not independent due to the constraints in Eq. (28). Thus, making

$$\{q\} = [T]^T \begin{bmatrix} -[\bar{C}^D]^{-1} [\bar{C}^I] \\ [I] \end{bmatrix} \{\bar{q}^I\} = [E] \{\bar{q}^I\} \quad (35)$$

and the dynamic equation of the original system is transformed into

$$[\bar{M}] \{\ddot{\bar{q}}^I\} + [\bar{D}] \{\dot{\bar{q}}^I\} + [\bar{K}] \{\bar{q}^I\} = \{\bar{F}\} \quad (36)$$

where $[\bar{M}] = [E]^T [M] [E]$, $[\bar{D}] = [E]^T [D] [E]$, $[\bar{K}] = [E]^T [K] [E]$ and $\{\bar{F}\} = [E]^T \{F\}$. Eq. (36) is the final governing equation of the blisk after introducing the constraints. It is obvious that Eq. (36) is $4 N_b$ fewer DOF than the original governing equation Eq. (32). After the MGMM proposed in this paper, the system is completely constrained, the singularity of the mass matrix does not appear, and even the dimension of the system decreases with the increase of the constraints. The advantage of improvement for traditional GMM in this paper is

that the singularity problem of the combined structure is eliminated, and the system becomes strictly positive definite, so that the analysis of the mode and dynamic response can be carried out directly without any treatment.

3. Convergence, experimental study and comparative analysis

3.1. Convergence in amplitude–frequency response

Before the analysis begins, it is necessary to verify the convergence of the proposed MGMM. In this subsection the convergence of the proposed MGMM is verified by studying the variation trend of the amplitude frequency response curve with the truncation number of the mode functions of the blade and disk in the span and radial direction. It should be pointed that, in the following analysis, $I^{Uz} = I^{U\phi} = I^{u\eta} = I^{u\phi}$ is assumed. Fig. 4 show amplitude–frequency response curves of 8-blades blisk system with different I^{Uz} , as well as the values of all relevant parameters. The information of excitation and response corresponding to Fig. 4 is that, unit harmonic excitation is applied at 75% of the span length of #1 blade, the damping factor of each mode is 0.001, and the coordinates of the response measurement point in disk is $r = 0.75 R^{out}$, $\theta = 0^\circ$. It can be seen from Fig. 4 that as I^{Uz} continues to increase, the overall amplitude–frequency curve gradually converges to a coincident curve, thus, the convergence of the proposed GMM is verified, and $I^{Uz} = I^{U\phi} = I^{u\eta} = I^{u\phi} = 25$ is given for the following analysis.

3.2. Verification with experiment

In this subsection, experiment and finite element method (FEM) are used to verify the accuracy of the proposed model by MGMM. The three-dimensional model of the blisk is shown in Fig. 5a. and there are 8 blades in the blisk. In order to ensure the applicability of the beam model for blades, high stiffness mass blocks are added at the joints of blades and disk, which results in the need to add additional kinetic energy in Eq. (29) when solving the Eq. (38), i.e

$$T^{block} = \frac{1}{2} \sum_{i=1}^{N_b} m^{block} \left(\dot{U}^z \Big|_{r_i} \right)^2 \quad (37)$$

In this experiment, the blisk model is made by 3D printing, the geometric size and material properties are shown in the Table 1.

The natural frequency of the blisk system can be calculated by the generalized eigenvalue problem of the mass matrix and stiffness matrix in Eq. (32), i.e.

$$([\bar{K}] - \lambda^2 [\bar{M}]) \{\bar{X}\} = \{0\} \quad (38)$$

where λ is the natural frequency of the blisk system. The eigen vector $\{\bar{X}\}$ of Eq. (38) characterize the mode shapes of system Eq. (36), and the eigen vector $\{X\}$ of original system Eq. (32) can be obtained by re-transformation, i.e. $\{X\} = [E] \{\bar{X}\}$.

The modal experiment adopts the method of “single-point excitation and multi-point measurement”, the excitation mode is sound excitation (see Fig. 5c), and the signal acquisition is PSV-500 Scanning Laser Vibrometer (SN:0217496, consisting of three laser scanning heads and a computer with corresponding software, see Fig. 5b), the Blisk is fixed to the base through the fixture (see Fig. 5c and d), and the exciter is placed behind one of the blades.

The natural frequency obtained by experiment, FEM and proposed MGMM are listed in Table 2. In FEM, SOLID186 element is used for the modal simulation of the Blisk.

It can be seen from Table 2 that the natural frequencies obtained by MGMM and FEM are in good agreement with those measured in the experiment, and the highest error of 8.51% between the FEM results and the experimental results occurs in the higher-order (17th order) mode. The maximum error between the results obtained by MGMM

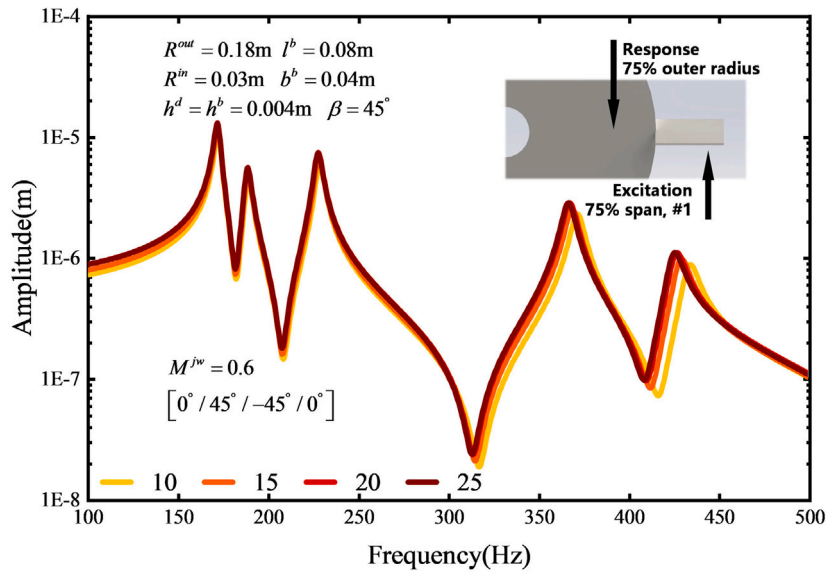


Fig. 4. Amplitude–frequency response curves when $I^{U^2} = 10, 15, 20, 25$ of the 8-blades blisk system.

Table 1

Parameters of the blades and disk for FEM and experiment.

	Geometry information	Material property
Disk	$R^{out} = 0.120\text{ m}$, $R^{in} = 0.020\text{ m}$, $h^d = 0.004\text{ m}$	$\rho^d = 1100\text{ kg/m}^3$, $E^d = 2.70\text{ GPa}$, $\nu^d = 0.42$
Blade	$l^b = 0.072\text{ m}$, $b^b = 0.03\text{ m}$, $h^b = 0.002\text{ m}$, $\beta = 45^\circ$	$\rho^b = 1100\text{ kg/m}^3$, $E^b = 2.70\text{ GPa}$, $\nu^b = 0.42$

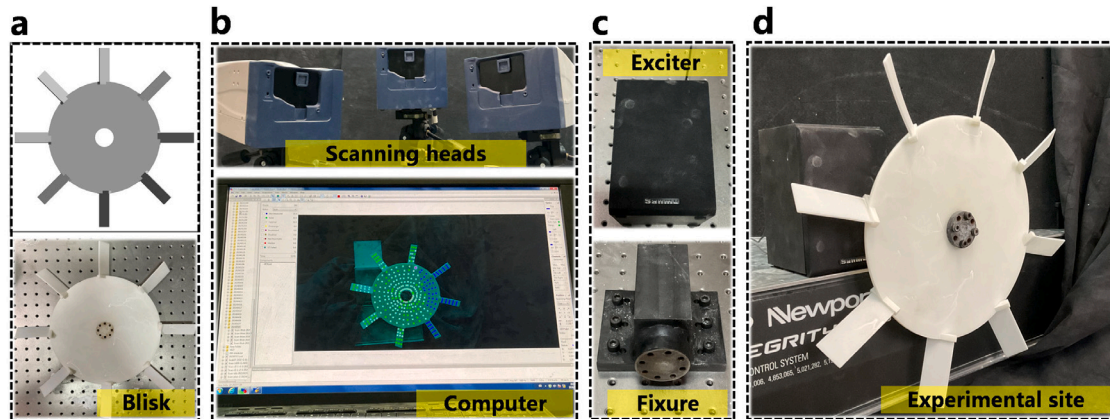


Fig. 5. Experimental equipment and experimental environment. a: digital model and solid model of blisk, b: PolyTec scanning header and computer, c: sound exciter and foundation, d: experimental site.

and those obtained by experiment occurs at the 14th order. However, the results of MGMM and FEM have a higher agreement, and the maximum error of 5.89% occurs in the 18th mode. The main sources of these errors are as follows: 1. manufacturing errors of materials such as structural mistuned and initial warping deformation of blisk; 2. The experimental device could not perfectly simulate the boundary condition of the disk with a fixed inner edge; 3. torsional mode shapes appear in the blades in higher order modes.

The mode shapes of the first 18 orders measured by MGMM, FEM and experiments are shown in Fig. 6. In the perfect blisk structure, there are modes with overlapping frequencies and orthogonal mode shapes, which have been reflected in Table 2, so only one of the modes with overlapping modes is illustrated in Fig. 6.

As can be seen from the comparison in Fig. 6, the mode shape obtained by MGMM are in good agreement with those obtained by FEM. It can be seen in Fig. 6 that in the first 8 modes, the first bending of the blade is coupled with the 1st, 0th, 2nd, 3rd, and 4th

nodal diameter mode of the disk, respectively. From the 9th to 16th modes, the second bend of the blade is coupled with the 1, 0, 2, 3, and 4 nodal diameter (ND) modes of the blade respectively. In the 17th and 18th modes, the second bend of the disk appears, coupling with the second order bending direction of the blade. The above coupling characteristics of blade and disk are reflected in the proposed MGMM, FEM and experimental results. Therefore, the correctness of the model by MGMM in this paper has been fully verified.

For the convenience of the following description, the mode shape of blisk is identified by the method of $D_m B_n$ according to the practice of [21], $D_m B_n$ stands for the mode shape of coupling mode between the m order ND shape of disk and the n order bending of blades. such as $D_1 B_1$ and $D_0 B_1$ corresponding the 1st and 3rd in Fig. 6. It should be pointed out that the case of 1st bending of the blade and 1st bending of the disk resulting 2nd bending of blisk occurs in the higher-order modes (such as 11th mode in Fig. 6), which should be collectively referred to as $D_m B_2$, hereafter.

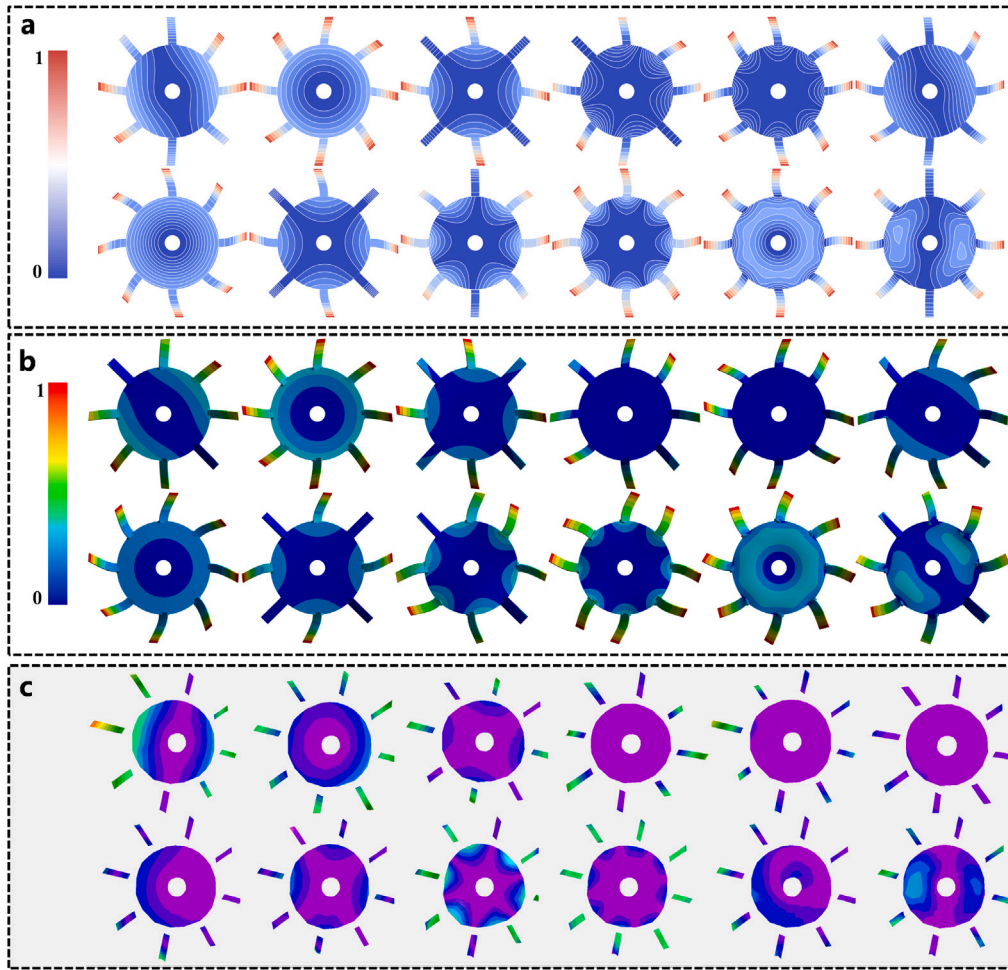


Fig. 6. Mode shapes of Experiment, FEM and MGMM, The order of modes in each subplot is 1,3,4,6,8,9,11,12,14,16,17,18 from left to right firstly and from top to bottom secondly a: Modes obtained by MGMM. b: Modes obtained by FEM. c: Modes obtained by experiment.

Table 2
Comparison of natural frequency results of FEM and MGMM.

Order	EXP (Hz)	FEM (Hz)	MGMM (Hz)	Error1 ^a	Error2 ^b	Error3 ^c
1	58.75	60	59.86	2.13%	1.89%	-0.23%
2	58.75	60	59.86	2.13%	1.89%	-0.23%
3	66.88	67.11	66.5	0.34%	-0.57%	-0.91%
4	71.88	69.58	69.06	-3.20%	-3.92%	-0.75%
5	71.88	69.58	69.06	-3.20%	-3.92%	-0.75%
6	87.1	87.89	86.61	0.91%	-0.56%	-1.46%
7	87.1	87.91	86.61	0.93%	-0.56%	-1.48%
8	91.56	90.95	89.58	-0.67%	-2.16%	-1.51%
9	112.24	114.43	113.48	1.95%	1.10%	-0.83%
10	112.24	114.45	113.48	1.97%	1.10%	-0.85%
11	118.44	116.43	116.03	-1.70%	-2.03%	-0.34%
12	131.56	123.21	122.98	-6.35%	-6.52%	-0.19%
13	131.56	123.22	122.98	-6.34%	-6.52%	-0.19%
14	185	173.84	169.74	-6.03%	-8.25%	-2.36%
15	185	173.85	169.74	-6.03%	-8.25%	-2.36%
16	225.94	210.87	208.74	-6.67%	-7.61%	-1.01%
17	286.25	310.61	300.72	8.51%	5.06%	-3.18%
18	331.56	330.19	310.75	-0.41%	-6.28%	-5.89%

^a Error between finite element results and experimental results, $(\lambda^{FEM} - \lambda^{EXP})/\lambda^{EXP}$.

^b Error between MGMM results and experimental results, $(\lambda^{MGMM} - \lambda^{EXP})/\lambda^{EXP}$.

^c Error between MGMM results and FEM results, $(\lambda^{MGMM} - \lambda^{FEM})/\lambda^{FEM}$.

3.3. Comparative analysis

In order to further reflect the advantages of MGMM proposed in this paper, in this subsection, a comparison between the results obtained by MGMM and the results obtained by the artificial spring (AS) method in [19] is carried out. There are 16 blades in the whole blisk, and the pre-setting angle of the blades is $\beta = 0^\circ$. For other geometric and material parameters, please refer to [19]. The results of the two methods and the finite element results in [19] are listed in Table 3.

As can be seen from the data in Table 3, the error of proposed MGMM results relative to the FEM is substantially smaller than the error of the AS method relative to the finite element in [19], and this advantage is particularly significant in high order modes. The reasons why the MGMM proposed in this paper can achieve more accurate results are as follows: firstly, MGMM can strictly satisfy the displacement continuity of the blade and disk, which is not possible with the artificial spring method; Secondly, Displacement field of blades and disk in this paper are built by high-order shear deformation theory, while the Euler–Bernoulli beam theory and Kirchhoff plate theory are used in [19].

4. Modal characteristics analysis

In this section, the modal characteristics of the 2D C/SiC composite blisk are analyzed in detail, including the effect of the rotational speed, the geometric parameters, the yarns density of arrangement in the single 2D C/SiC materials, and the laying scheme of the lamination

Table 3
Comparison of results (proposed MGMM and artificial spring method of [19]).

Mode	Ref. [19] FEM (Hz)	Ref. [19] method of artificial spring(AS) (Hz)	MGMM (Hz)	Error1 ^a	Error2 ^b
D_1B_1	174.52	174.16	174.38	-0.21%	-0.08%
D_2B_1	196.13	194.19	194.48	-0.99%	-0.84%
D_3B_1	263.18	255.22	258.47	-3.02%	-1.79%
D_4B_1	351.78	323.74	347.03	-7.97%	-1.35%
D_5B_1	426.62	392.96	429.22	-7.89%	0.61%
D_6B_1	476.64	434.86	494.07	-8.77%	3.66%
D_1B_2	796.14	713.02	822.17	-10.44%	3.27%
D_2B_2	843.37	751.93	874.68	-10.84%	3.71%
D_3B_2	946.56	845.23	983.64	-10.71%	3.92%
D_4B_2	1126.04	1053.11	1161.84	-6.48%	3.18%
D_5B_2	1382.66	1260.97	1402.21	-8.80%	1.41%
D_6B_2	1693.53	1552.93	1678.52	-8.30%	-0.89%

^a Error between method of AS in [19] and FEM in [19], $(\lambda^{AS} - \lambda^{FEM})/\lambda^{FEM}$.
^b Error between proposed MGMM and FEM in [19], $(\lambda^{MGMM} - \lambda^{FEM})/\lambda^{FEM}$.

Table 4
Geometry parameters of the blades and disk for parameter analysis.

	Geometry information of blisk	Geometry information of single 2D C/SiC composite
Disk	$R^{out} = 0.180$ m, $R^{in} = 0.030$ m, $h^d = 0.004$ m	
Blade	$b^b = 0.04$ m, $h^b = 0.004$ m	$b^{jw} = 0.9$ mm, $h^{jw} = 0.12$ mm, $d = 0.08$ mm, $L^z = 0.5$ mm

structure on the natural frequency of the blisk and the resulting modal steering phenomenon.

The geometry of the disk in this section is shown in Table 4, parameters of Table 4 do not change during the analysis, and the material information of the C fiber and SiC matrix is listed in Appendix.

4.1. Effect of yarns density of arrangement on modal characteristics

In this subsection, the laying scheme is $[0^\circ/45^\circ/-45^\circ/0^\circ]$, blade span $l^b = 0.080$ m and pre-setting angle $\beta = 45^\circ$ are given, and the yarns density of arrangement is taken into analysis of effect on modal characteristics. Firstly it is necessary to be pointed out that M^{jw} has a decisive influence on the volume fraction of yarns, so the analysis in this subsection sets the upper limit of M^{jw} to 1 tows/mm to avoid an excessively high fiber volume fraction.

The effect of yarns density on natural frequency is shown in Fig. 7, as well as the type of mode shapes. It can be seen clearly that the natural frequency from 1 to 16 order all decrease on a considerable scale as the yarns density of arrangement M^{jw} increases, this is because with the increase of M^{jw} , the yarns gradually occupies a dominant position in RVE, and its contribution proportion to the stiffness of RVE increases. While the stiffness of yarn is smaller than the stiffness of SiC matrix, which leads to the decrease of the stiffness of 2D C/SiC composite and the decrease of the natural frequency. Fig. 7c shows the percentage of decrease of the first 16 natural frequency, obviously, the difference of the influence of yarns density of arrangement on each order of frequency varies very little, ranging from 9.0% to 9.5% (the maximum is 9.32%, the minimum is 9.05%).

4.2. Effect of laying scheme on modal

In this subsection, yarns density of arrangement $M^{jw} = 0.6$ tows/mm, blade span $l^b = 0.080$ m and pre-setting angle $\beta = 45^\circ$ are given with analysis. Considering that there are 8 blades in blisk, the laying scheme is adopted as the following 2 scheme: $[0/\tau]_s$, $[0/\tau]_{as}$, $[0/\tau/45/\tau + 45^\circ]_s$ and $[0/\tau/45/\tau + 45^\circ]_{as}$, where “s” and “as” stands for symmetric and anti-symmetric laying, τ stands for adjustable angle. the influence of different τ of the 2 laying scheme on the natural frequency of blisk is investigated in this subsection.

Fig. 8 shows the change curve of the natural frequency of each order as τ increases from 0° to 90° , the change curve of the natural frequency of each order is marked with the corresponding mode shapes D_mB_n in each sub-figure in Fig. 8. First of all, the most noteworthy phenomenon

is that in these 4 laying schemes, there is a separation of D_2 mode shape of disk. In Fig. 8a, the natural frequencies corresponding to the same mode shape of D_2B_1 and D_2B_2 are separated. For a more in-depth explanation, modal assurance criterion (MAC) is introduced in this subsection, which is expressed as

$$MAC(i, j) = \lg \frac{(\{X_i\}^T \{X_j\})^2}{(\{X_i\}^T \{X_i\})(\{X_j\}^T \{X_j\})} \quad (39)$$

where $\{X_i\}$ stands for i th mode vector, MAC characterizes the similarity of different modes. The MAC values of D_2B_1 mode and D_2B_2 mode of Scheme 1(S) and Scheme 2(s) are illustrated in Fig. 8b2 - b3, and for contrast, the MAC values of blisk of isotropic pure SiC are also shown in Fig. 8b1. It can be seen from Fig. 8b that in the isotropic case of SiC blisk, the MAC of the two coincident modes of D_2B_1 and D_2B_2 is -2.3 and -3.2 , respectively, while in scheme 1(S) and scheme 2(S), the MAC drops rapidly to within the range of the mechanical error, which fully demonstrates that the mode separation of D_2 of disk is indeed caused by the anisotropy of the single-layer C/SiC material. This is because the single layer material in this paper is not strictly isotropic in the plane where the disk is located, and its two principal materials axis with the same mechanical properties are orthogonal to each other in the plane of disk. This also leads to a small range of fluctuations in the natural frequencies of each order as τ increases from 0° to 90° . In addition, it can also be seen from Fig. 8 that the frequency of each order of the first laying scheme $[0^\circ/\tau]_s$ and $[0^\circ/\tau]_{as}$ is slightly higher than that of the second laying scheme $[0/\tau/45/\tau + 45^\circ]_s$ and $[0/\tau/45/\tau + 45^\circ]_{as}$ (except for the separating mode D_2B_1 and D_2B_2), and all of them reach the minimum when $\tau = 45^\circ$. The influence of the asymmetrical laying mode and the anti-symmetrical laying scheme on the natural frequency of each order is very small and can be almost ignored.

4.3. Effect of rotational speed on modal characteristic

The mode steering of a rotor system due to speed variation has always been a classical problem in rotor dynamics. In this subsection, the laying scheme is given as $[0^\circ/45^\circ/-45^\circ/0^\circ]$, and $l^b = 0.08m$, $\beta = 45^\circ$. The rotational speed is taken into parameter analysis, other parameters are still shown in Table 4. Curves of natural frequency of blisk as a function of rotational speed with different yarns density of arrangement are illustrated in Fig. 9. Firstly, the phenomenon of increasing natural frequency caused by centrifugal stiffening occurs in every mode of blisk. Mode steering due to the increase of rotational speed occurs in the

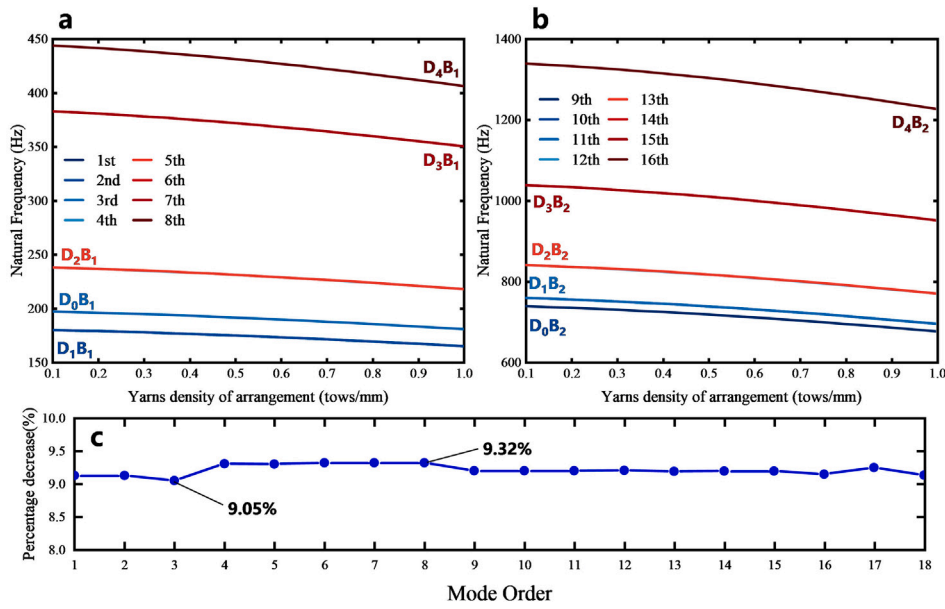


Fig. 7. Effect of yarns density of arrangement on modal characteristics a:Natural frequencies of 1–8 order. b:Natural frequencies of 9–16 order. c:Percentage of decrease of 1 to 16 order of frequency as M^{Jw} increases from 0.1 to 1.

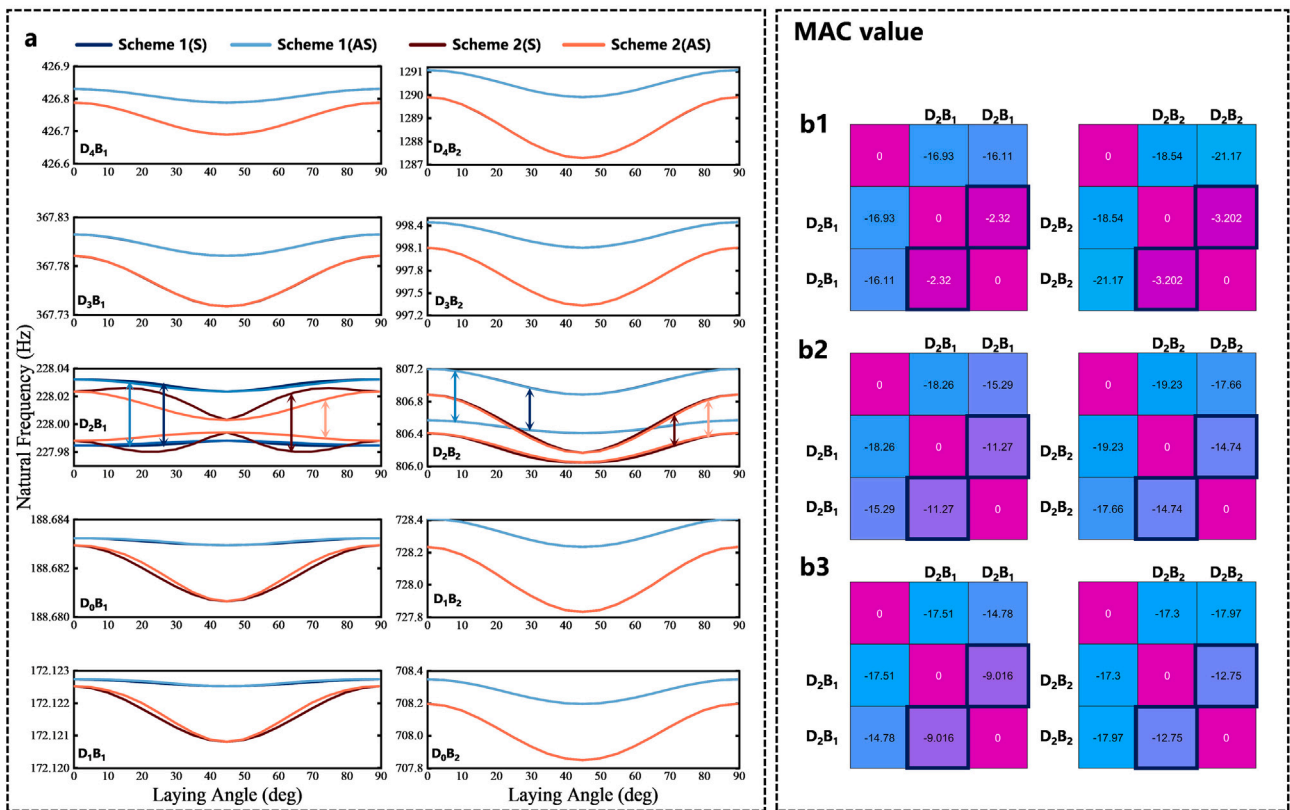


Fig. 8. Effect of laying Scheme of lamination on modal characteristics from 1 to 16 order when $M^{Jw} = 0.6$. a: “Scheme1(S)” and “Scheme1(AS)” stand for $[0/\tau]_s$ and $[0/\tau]_{as}$, “Scheme2(S)” and “Scheme2(AS)” stand for $[0/\tau/45/\tau + 45^\circ]_s$ and $[0/\tau/45/\tau + 45^\circ]_{as}$. b1:MAC values of isotropic pure SiC blisk modal when $\tau = 45^\circ$. b2:MAC values of blisk modal of scheme 1(S) when $\tau = 45^\circ$. b3:MAC values of blisk modal of scheme 2(S) when $\tau = 45^\circ$.

first 3 modes of the first mode set (see Fig. 9b), the mode shapes change from D_1B_1, D_0B_1 in lower rotational speed into D_0B_1, D_1B_1 in higher rotational speed (see Fig. 9c). At the same time, it can also be seen from Fig. 9b that the increase of M^{Jw} leads to the advance of the mode steering point in addition to the decrease of the natural frequencies of each order.

4.4. Effect of ratio of blade span to disk outer radius on modal characteristics

In this subsection, the laying scheme of lamination structure is given as $[0^\circ/45^\circ/-45^\circ/0^\circ]$, and $\beta = 45^\circ$. The span length of blades are taken into parameter analysis, and the other parameters are still given in

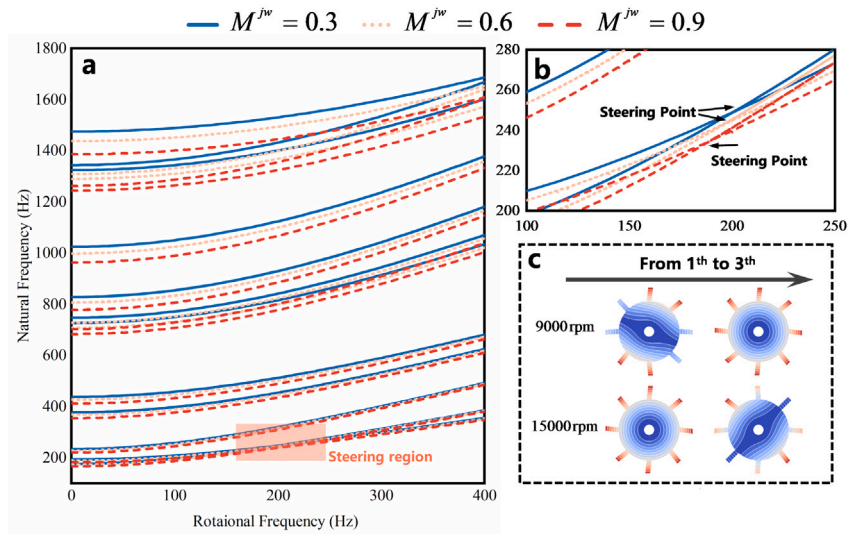


Fig. 9. Effect of rotational frequency on modal characteristics without gyro damping. a: The global graph. b: The sub region of steering of a. c: Modal steering at 9000 rpm (150 Hz) and 15000 rpm (250 Hz).

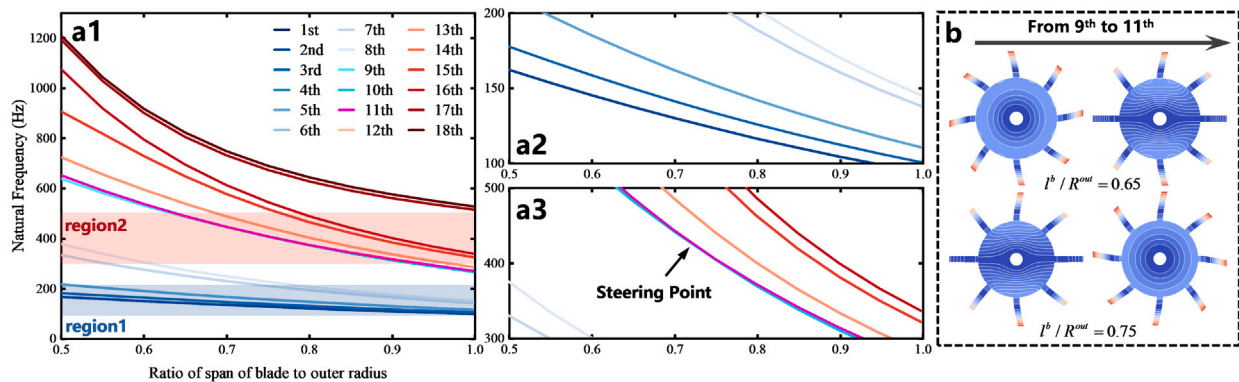


Fig. 10. Effect of the ratio of blade span to disk outer radius. a1: natural frequencies from 1 to 18 order. a2: local graph of region 1 of a1. a3: local graph of region 2 of a1. b: frequency steering in a3. A modal steering takes place between 0.65 and 0.75 of the ratio of blade span to disk outer radius.

Table 4. Fig. 10 illustrates the effect of the ratio of blade span to disk outer radius on the natural frequencies of each order. It can be seen from Fig. 10 that as l^b/R^{out} increases the modes of each order decrease, but the decrease of second mode set (9th to 16th) is significantly larger than that of the first mode set (1st to 8th, see Fig. 10a), and mode steering phenomenon occurs among the 9th and 10th of the second mode set, as shown in Fig. 10a3. When $l^b/R^{out} = 0.65$, the 9th and 10th are D_0B_2 and D_1B_2 , respectively. When $l^b/R^{out} = 0.75$, the 9th (10th) and 11th order are D_1B_2 and D_0B_2 , respectively. Additionally, no mode steering occurs for the higher-order modes 17th and 18th and for the first family of modes.

4.5. Effect of pre-setting angle on modal characteristics

In this subsection, the laying scheme of lamination structure is also given as $[0^\circ/45^\circ/-45^\circ/0^\circ]$, the blade span is $l^b = 0.08\text{m}$, the pre-setting angle is taken into parameter analysis, the other parameters are still given in Table 4.

The effect of pre-setting angle of the blades on natural frequency is illustrated in Fig. 11a. The frequency of first modal set (1st to 8th in Fig. 11a2) increases slowly as pre-setting angle β increases. However, the individual frequencies in second modal set and high-order (9th to 18th in Fig. 11a3) have different development trend with the increase of β , and some of them converges to the same value as β approaches

90° , and modal steering takes place in 16th, 17th, 18th within 35° to 55° (see Fig. 11b).

In order to explain the phenomenon that development trend of the modes of different orders in the second mode set is not consistent, the mode shape diagram with $\beta = 70^\circ, 80^\circ, 90^\circ$ in Fig. 11a3 region 3 is shown in Fig. 11c. It can be seen from Fig. 11c that, from 9th to 18th, the first three modes D_0B_2, D_1B_2, D_2B_2 do not change during the increase of β , while in the later modes, when β reaches 90° , these modes degenerate into the single cantilever blade mode. In the model proposed of this paper, there is no circumferential torsional deformation of the disk, i.e., the disk is rigid in the circumferential direction, so the lateral displacement of the blades is independent of each other when β is 90° , and the blades degenerate independent cantilever blades. The development trend of these modes degenerated into a single cantilever blade depends on the value of the natural frequency of the single cantilever blade, which leads to the phenomenon that development trend of several modes is not consistent, and several modes converge to the same value. At the same time, in the process of increasing β , the motion coupled with the lateral motion of disk gradually changes from the lateral motion of the blade to the chord-wise motion of blades, which means that, with the increase of β , the stiffness of blisk in the lateral direction gradually increases. So the first modes set and the non-degenerating modes of second modes set increase with the increase of β .

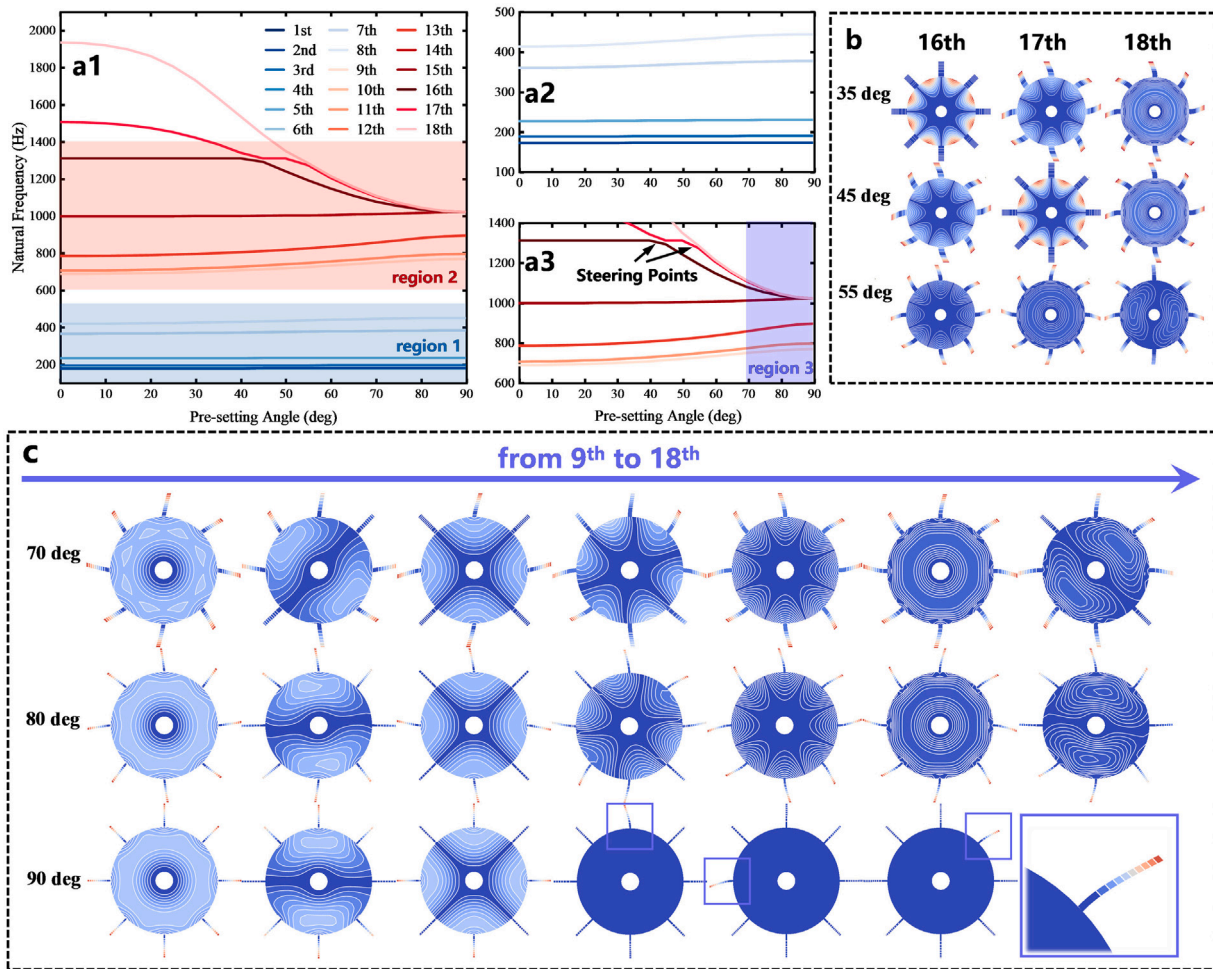


Fig. 11. Effect of the pre-setting angle on modal characteristics. a1: effect of pre-setting angle of blades on natural frequencies from 1 to 8 order. a2: local graph of region 1 of a1. a3: local graph of region 2 of a1. b: two modal steering takes place between 35° and 55° of the pre-setting angle β c: mode shapes from 9th to 18th in a3 region 3.

5. Conclusion and final remarks

In this paper, an improved global mode method has been proposed, which is semi-analytical and suitable for the dynamic modeling of composite blisk. Combined with the high-order shear deformation theory and Hamilton’s principle, the dynamic modeling of 2D C/SiC composite blisk has been completed, and then the finite element simulation and experimental studies have been carried out to verify the accuracy of proposed method. Finally, the analysis of geometric and materials parameters of blisk has been carried out under the framework of the proposed method. Some valuable conclusions are as follows.

In the MGMM proposed in this paper, the connection between blade and disk is no longer handled by the traditional Lagrange multiplier method, but by multi-modal transformation to transform the system to another modal space to eliminate the constrained coordinates. The improvement of the traditional GMM in this paper has the advantage of eliminating the singularity caused by the introduction of Lagrange multipliers, which not only improves the stability of the numerical solution but also eliminates the need for mode extraction and reconstruction before dynamic response analysis. Compared with the previous modeling methods for the blisk, the proposed method has higher mechanical and physical rationality, and is more suitable for the modeling of composite structures because of the use of high-order shear deformation constitutive.

The convergence and correctness of the proposed method have been verified. The convergence of the proposed modified global mode method is verified by the convergence of the amplitude–frequency response. The results of the finite element simulation and modal experiment for the blisk are highly consistent with mode shape obtained by the MGMM. The results of the natural frequency obtained by the three methods are in good agreement, and the errors are mainly concentrated in the high order modes.

Based on the frame of MGMM proposed, the parameters analysis has been carried out. In the example of this paper, among the material and lay-up parameters of 2D C/SiC, the yarns density of arrangement has the greatest influence on the modal characteristics of blisk. When yarns density of arrangement increases from 0.1 to 1 tows/mm, the natural frequencies of each order decrease by 9% to 10%. However, the laying scheme has little influence on the modal characteristics, and the natural frequency of Blisk fluctuates within a small range due to the change of laying Angle. In addition, since 2D C/SiC is not strictly isotropic in the plane of Blisk, the 2ND modes of the blisk are slightly separated, and the change of material parameters do not lead to the phenomenon of mode steering.

Geometric parameters have great influence on the modal characteristics of the blade, including the rotational speed, the ratio of the blade span to disk outer radius, and the pre-setting angle of the blades. The order of the mode steering caused by the change of geometric

Table A.1
Material parameters of C and SiC.

Materials	density	Elastic parameters
C fiber	1600 kg/m ³	$E_1 = 211$ GPa, $E_2 = 13.8$ GPa, $G_{12} = 9$ GPa, $G_{23} = 4.8$ GPa, $\nu_{12} = 0.2$, $\nu_{23} = 0.25$
SiC matrix	3200 kg/m ³	$E = 350$ GPa, $\nu = 0.25$

parameters is not consistent. The mode steering due to the rotational speed occurs in the first mode set, and the mode steering due to the ratio of the blade span to the disk outer radius and the pre-setting angle occurs in the second mode set.

Code and data availability

Data will be made available on request.

CRediT authorship contribution statement

Qian Xu: Writing – original draft, Validation, Software, Methodology, Investigation, Formal analysis, Data curation. **Lei Hou:** Project administration, Funding acquisition, Conceptualization. **Lixian Hou:** Writing – review & editing, Writing – original draft. **Zhonggang Li:** Writing – review & editing, Software. **Shuangxing Ren:** Writing – review & editing, Methodology. **Mohamed K. Aboudaif:** Funding acquisition. **Emad Mahrous Awwad:** Funding acquisition. **Nasser A. Saeed:** Funding acquisition.

Declaration of competing interest

The authors declare that they have no conflict of interest.

Data availability

No data was used for the research described in the article.

Acknowledgments

It is very grateful for the National Natural Science Foundation of China (Grant No. 12372008), the National Key R&D Program of China (Grant No. 2023YFE0125900), the Natural Science Foundation of Heilongjiang Province (Outstanding Youth Foundation, Grant No. YQ2022A008). The authors are grateful to the Raytheon Chair for Systems Engineering for funding.

Appendix. Material parameters of C fiber and SiC matrix

The material parameters of C fiber and SiC matrix are shown in Table A.1.

References

- [1] Yi Chen, Lei Hou, Guo Chen, Huiying Song, Rongzhou Lin, Yuhong Jin, Yushu Chen, Nonlinear dynamics analysis of a dual-rotor-bearing-casing system based on a modified HB-AFT method, *Mech. Syst. Signal Process.* 185 (2023) 109805.
- [2] Zeyuan Chang, Lei Hou, Rongzhou Lin, Yuhong Jin, Yushu Chen, A modified IHB method for nonlinear dynamic and thermal coupling analysis of rotor-bearing systems, *Mech. Syst. Signal Process.* 200 (2023) 110586.
- [3] RongZou Lin, Lei Hou, ShiWei Dun, YuFeng Cai, ChuanZong Sun, YuShu Chen, Synchronous impact phenomenon of a high-dimension complex nonlinear dual-rotor system subjected to multi-frequency excitations, *Sci. China Technol. Sci.* 66 (6) (2023) 1757–1768.
- [4] Kunpeng Xu, Wei Sun, Junnan Gao, Mistuning identification and model updating of coated blisk based on modal test, *Mech. Syst. Signal Process.* 121 (2019) 299–321.
- [5] Kunpeng Xu, Wei Sun, Xianfei Yan, Jin Wang, Damping mistuning identification of coated blisks by means of vibrational test, *J. Sound Vib.* 463 (2019) 114954.
- [6] M.R. Effinger, R.C. Clinton, J. Dennis, S. Elam, G. Genge, A. Eckel, M.H. Jaskowiak, J.D. Kiser, J. Lang, Fabrication and testing of ceramic matrix composite rocket propulsion components, 2001.
- [7] W. Zhang, L. Ma, Y.F. Zhang, K. Behdinan, Nonlinear and dual-parameter chaotic vibrations of lumped parameter model in blisk under combined aerodynamic force and varying rotating speed, *Nonlinear Dynam.* 108 (2) (2022) 1217–1246.
- [8] W. Sun, R. Li, J.X. Jiang, Lumped-parametric modeling based on modal test and analysis of vibration characteristics of the hard-coated blisk, *J. Vib. Eng. Technol.* 7 (4) (2019) 347–358.
- [9] Javier González-Monge, Salvador Rodríguez-Blanco, Carlos Martel, Nonlinear switching between flutter and forced response in bladed disks, *Nonlinear Dynam.* 111 (6) (2023) 5237–5247.
- [10] Animesh Chatterjee, Lumped parameter modelling of turbine blade packets for analysis of modal characteristics and identification of damage induced mistuning, *Appl. Math. Model.* 40 (3) (2016) 2119–2133.
- [11] Daosen Liang, Zichu Jia, Zhifu Cao, Yulin Wu, Rui Zhang, Jun Fan, Changyao Wu, Jianyao Yao, Geometric mistuning identification and finite element model updating methods for bladed disks, *Aerosp. Sci. Technol.* 130 (2022) 107915.
- [12] Feng Gao, Wei Sun, Vibration characteristics and damping analysis of the blisk-deposited hard coating using the Rayleigh-Ritz method, *Coatings* 7 (8) (2017) 108.
- [13] Daitong Wei, Hongkun Li, Yugang Chen, Xinwei Zhao, Jiannan Dong, Zhenfang Fan, A novel model reduction technique for mistuned blisks based on proper orthogonal decomposition in frequency domain, *Aerosp. Sci. Technol.* 121 (2022) 107320.
- [14] Wu Ce Xing, Yan Qing Wang, Dynamic modeling and vibration analysis of bolted flange joint disk-drum structures: Theory and experiment, *Int. J. Mech. Sci.* 272 (2024) 109186.
- [15] Zhaoye Qin, Zhengbao Yang, Jean Zu, Fulei Chu, Free vibration analysis of rotating cylindrical shells coupled with moderately thick annular plates, *Int. J. Mech. Sci.* 142–143 (2018) 127–139.
- [16] Guodong Jin, Lei Ma, Hong Zhang, Qingshan Wang, Vibration characteristics analysis of composite laminated annular/circular plate using high-order shear deformation theory, *Shock Vib.* 2021 (2021) e5913860.
- [17] T. Tomioka, Y. Kobayashi, G. Yamada, Analysis of free vibration of rotating disk-blade coupled systems by using artificial springs and orthogonal polynomials, *J. Sound Vib.* 191 (1) (1996) 53–73.
- [18] Feng Gao, Wei Sun, Junnan Gao, Forced vibration analysis of the hard-coating blisk considering the strain-dependent manner of the hard-coating damper, *Aerosp. Sci. Technol.* 79 (2018) 187–198.
- [19] Yugang Chen, Jingyu Zhai, Qingkai Han, Vibration and damping analysis of the bladed disk with damping hard coating on blades, *Aerosp. Sci. Technol.* 58 (2016) 248–257.
- [20] Xiaojun Guo, Youliang Xu, Jian Li, Xiao Luo, Longbiao Li, Xiaohan Hu, Damage monitoring of SiC/SiC turbine blisk under overspeed rotation testing using X-ray computed tomography and natural frequency, *Proc. Inst. Mech. Eng. L* (2023) 14644207231205875.
- [21] Zhi-Yuan Wu, Han Yan, Lin-Chuan Zhao, Ge Yan, Ao Chen, Hai-Feng Hu, Wen-Ming Zhang, Influences of blade crack on the coupling characteristics in a bladed disk with elastic support, *Aerosp. Sci. Technol.* 133 (2023) 108135.
- [22] Zhi-Yuan Wu, Han Yan, Lin-Chuan Zhao, Ge Yan, Ao Chen, Wen-Ming Zhang, Modal characteristics of a flexible dual-rotor coupling system with blade crack, *J. Sound Vib.* 567 (2023) 118061.
- [23] Yi-Jui Chiu, Dar-Zen Chen, The coupled vibration in a rotating multi-disk rotor system, *Int. J. Mech. Sci.* 53 (1) (2011) 1–10.
- [24] S.B. Chun, C.W. Lee, Vibration analysis of shaft-bladed disk system by using substructure synthesis and assumed modes method, *J. Sound Vib.* 189 (5) (1996) 587–608.
- [25] Houxin She, Chaofeng Li, Qiansheng Tang, Bangchun Wen, Veering and merging analysis of nonlinear resonance frequencies of an assembly bladed disk system, *J. Sound Vib.* 493 (2021) 115818.
- [26] Tianyu Zhao, Yu Ma, Hongyuan Zhang, Jie Yang, Coupled free vibration of spinning functionally graded porous double-bladed disk systems reinforced with graphene nanoplatelets, *Materials* 13 (24) (2020) 5610.
- [27] Tian Yu Zhao, Yu Ma, Hong Yuan Zhang, Hong Gang Pan, Yi Cai, Free vibration analysis of a rotating graphene nanoplatelet reinforced pre-twist blade-disk assembly with a setting angle, *Appl. Math. Model.* 93 (2021) 578–596.
- [28] Shui-Ting Zhou, Yi-Jui Chiu, Guo-Fei Yu, Chia-Hao Yang, Hong-Wu Huang, Sheng-Rui Jian, An assumed mode method and finite element method investigation of the coupled vibration in a flexible-disk rotor system with lacing wires, *J. Mech. Sci. Technol.* 31 (2) (2017) 577–586.
- [29] Lun Liu, Dengqing Cao, Xiaojun Tan, Studies on global analytical mode for a three-axis attitude stabilized spacecraft by using the Rayleigh-Ritz method, *Arch. Appl. Mech.* 86 (12) (2016) 1927–1946.

- [30] Jin Wei, Dengqing Cao, Lianchao Wang, Hua Huang, Wenhui Huang, Dynamic modeling and simulation for flexible spacecraft with flexible jointed solar panels, *Int. J. Mech. Sci.* 130 (2017) 558–570.
- [31] Jin Wei, Dengqing Cao, Lun Liu, Wenhui Huang, Global mode method for dynamic modeling of a flexible-link flexible-joint manipulator with tip mass, *Appl. Math. Model.* 48 (2017) 787–805.
- [32] Yuteng Cao, Dengqing Cao, Jin Wei, Wenhui Huang, Modeling for solar array drive assembly system and compensating for the rotating speed fluctuation, *Aerosp. Sci. Technol.* 84 (2019) 131–142.
- [33] Guiqin He, Dengqing Cao, Yuteng Cao, Wenhui Huang, Investigation on global analytic modes for a three-axis attitude stabilized spacecraft with jointed panels, *Aerosp. Sci. Technol.* 106 (2020) 106087.
- [34] Guiqin He, Dengqing Cao, Yuteng Cao, Wenhui Huang, Dynamic modeling and orbit maneuvering response analysis for a three-axis attitude stabilized large scale flexible spacecraft installed with hinged solar arrays, *Mech. Syst. Signal Process.* 162 (2022) 108083.
- [35] Kaiyuan Tian, Yilong Wang, Dengqing Cao, Kaiping Yu, Approximate global mode method for flutter analysis of folding wings, *Int. J. Mech. Sci.* 265 (2024) 108902.
- [36] Hisaichi Ohnabe, Shoju Masaki, Masakazu Onozuka, Kaoru Miyahara, Tadashi Sasa, Potential application of ceramic matrix composites to aero-engine components, *Composites A* 30 (4) (1999) 489–496.
- [37] Hui Mei, Laifei Cheng, Comparison of the mechanical hysteresis of carbon/ceramic-matrix composites with different fiber preforms, *Carbon* 47 (4) (2009) 1034–1042.
- [38] Fumiaki Watanabe, Takeshi Nakamura, Ken-ichi Shinohara, The application of ceramic matrix composite to low pressure turbine blade, in: *ASME Turbo Expo 2016: Turbomachinery Technical Conference and Exposition*, American Society of Mechanical Engineers, 2016, V006T02A003.
- [39] Keqiang Zhang, Lu Zhang, Rujie He, Kaiyu Wang, Kai Wei, Bing Zhang, Joining of C_f /SiC ceramic matrix composites: A review, *Adv. Mater. Sci. Eng.* 2018 (2018) 1–15.
- [40] Ningkun Liu, Lingjun Guo, Gang Kou, Yunyu Li, Xuemin Yin, Ablation behavior of thin-blade co-deposited C/Cx-SiCy composites under the influence of the complex fluid conditions of the oxyacetylene torch, *Ceram. Int.* 48 (12) (2022) 16923–16932.
- [41] Florence Nyssen, Nicolas Tableau, Deborah Lavazec, Alain Batailly, Experimental and numerical characterization of a ceramic matrix composite shroud segment under impact loading, *J. Sound Vib.* 467 (2020) 115040.
- [42] James Min, Donald Harris, Joseph Ting, Advances in ceramic matrix composite blade damping characteristics for aerospace turbomachinery applications, in: *52nd AIAA/ASME/ASCE/AHS/ASC Structures, Structural Dynamics and Materials Conference*, American Institute of Aeronautics and Astronautics, 2011.
- [43] Rajesh S. Kumar, Analysis of coupled ply damage and delamination failure processes in ceramic matrix composites, *Acta Mater.* 61 (10) (2013) 3535–3548.
- [44] Nisrene Langenbrunner, Matt Weaver, Michael G. Dunn, Corso Padova, Jeffery Barton, Dynamic response of a metal and a CMC turbine blade during a controlled rub event using a segmented shroud, *J. Eng. Gas Turbines Power* 137 (6) (2015) 062504.
- [45] Guang-Hai Liu, Lai-Fei Cheng, Xin-Gang Luan, Yong-Sheng Liu, Self-healing behavior of 2D-C/[SiC-(B-C)] composite in aero-engine combustion chamber, *J. Inorg. Mater.* 26 (9) (2011) 969–973.
- [46] H. Mei, L.F. Cheng, L.T. Zhang, X.G. Luan, J. Zhang, Behavior of two-dimensional C/SiC composites subjected to thermal cycling in controlled environments, *Carbon* 44 (1) (2006) 121–127.
- [47] Xuefeng Teng, Shuangqi Lyu, Xiaohan Hu, Yun Jiang, Xiangfan Nie, Xin Liu, Longbiao Li, Effect of off-axis angle on mesoscale deformation and failure behavior of plain-woven C/SiC composites with digital image correlation, *J. Eur. Ceram. Soc.* 42 (12) (2022) 4712–4722.
- [48] Diantang Zhang, Li Chen, Yanjie Wang, Likai Zhang, Yifan Zhang, Kejing Yu, Xuefeng Lu, Jie Sun, Xueliang Xiao, Kun Qian, Stress field distribution of warp-reinforced 2.5D woven composites using an idealized meso-scale voxel-based model, *J. Mater. Sci.* 52 (11) (2017) 6814–6836.
- [49] V.G. Belardi, P. Fanelli, F. Vivio, Bending analysis with Galerkin method of rectilinear orthotropic composite circular plates subject to transversal load, *Composites B* 140 (2018) 250–259.
- [50] Hao Liu, Yegao Qu, Hao Gao, Fangtao Xie, Guang Meng, Nonlinear aeroelastic fluid-structure-acoustic interaction analysis of a coupled composite panel with an acoustic cavity in supersonic flow, *J. Sound Vib.* 569 (2024) 118086.
- [51] Dengqing Cao, Yang Yang, Huatao Chen, Deyou Wang, Guangyi Jiang, Cheng-gang Li, Jin Wei, Kun Zhao, A novel contact force model for the impact analysis of structures with coating and its experimental verification, *Mech. Syst. Signal Process.* 70–71 (2016) 1056–1072.